ELSEVIER

International Journal of Mass Spectrometry 215 (2002) 13–30

International Journal of Mass Spectrometry

www.elsevier.com/locate/ijms

The ion detection efficiency of microchannel plates (MCPs)

G.W. Fraser

Department of Physics and Astronomy, Space Research Centre, University of Leicester, University Road, Leicester LE1 7RH, UK

Received 9 October 2001; accepted 14 November 2001

Abstract

General expressions are derived for the detection efficiency of microchannel plate ion detectors. The model, based on earlier calculations for electrons and soft X-rays, accounts for the energy, incident angle, mass, electronic charge and nuclear charge of the ion and for the electrical and geometric parameters of the microchannels. The underlying dependence of the ion detection efficiency on ion velocity is derived from first principles. The initial predictions of the model are compared with measurements taken from the literature. Calculated efficiency-versus-angle, efficiency-versus-energy and efficiency-versus-mass curves are presented. The first calculations of the MCP efficiency for high mass ions (up to 100,000 u) are reported. We describe the extension of the model from "bare" MCPs, in which the active surfaces are the lead silicate glass of the channel walls and the nickel-based electrodes at the channel entrance and exit, to the case of alkali halide-coated plates. (Int J Mass Spectrom 215 (2002) 13–30)

Keywords: Microchannel plate; Detection efficiency; Kinetic and potential emission; Macromolecular ions

1. Introduction

Microchannel plate (MCP) electron multipliers, manufactured from lead silicate glass, are used as imaging ion detectors in applications ranging from the in situ analysis of space plasmas to field ion microscopy to the laboratory-based mass spectrometry of both low-mass and macromolecular (∼5–100 kDa) species.

There are many published measurements of the ion detection efficiency of MCPs ([1–30], Table 1). It is, however, impossible to derive from the available data a complete picture of the underlying efficiency function:

$$Q_i(\theta, \theta_B, E, Z_i, n, V_o, V_{coll}, L, h, D, A_{open})$$

counts/incident ion

Here, an ion with atomic number Z_i, kinetic energy E (velocity v) and bearing an electronic charge n is incident at an angle θ to the axis of a microchannel of diameter D and length L. The bias angle of the channel (the angle between the channel axis and the normal to the MCP front surface) is θ_B. The nickel-based (nichrome or inconel) electrodes on the input and output faces of the MCP penetrate h channel diameters into the channels: h can also denote the channel penetration depth of an alkali halide coating evaporated onto the plate in order to increase the ion detection efficiency. The channels are arranged, as shown in Fig. 1(a), in a regular hexagonally-packed array of pitch p and open area fraction A_{open}, where [31]:

$$A_{open} = \left(\frac{2\pi}{\sqrt{3}}\right)\left(\frac{D}{2p}\right)^2 \quad (1)$$

E-mail: gwf@star.le.ac.uk

1387-3806/02/$20.00
PII S1387-3806(01)00553-X

Table 1
Experimental arrangements for the measurement of Q_i[a]

Reference	θ_B (°)	V_o (kV)	Species and charge state (if $n \neq 1$)	E (keV)
[1]	5, 15	1.0	Ar	20
[2]	8	0.9	C^{4+}, N^{5+}, O^{5-8+}, F^{7+}, Ne^{5-9+}	Velocity range 3–4.5 × 10^5 m s^{-1}
[3]	11	0.95	H, He, O	0.25–5
	A_{open} = 0.55; L/D = 40:1 (assumed); h = 0.5 (assumed); no front surface contribution			
[4]	13	–	He, Ne, Ar	3–25
[5]	–	1.0	Mo^{2-4+}, Re^{3+}	–
[6]	10	1.0	Mg	2.1–4.4
[7]	–	–	He, Ne, Ar	3–25
[8]	–	–	He	1–10
[9]	10	0.76	Ne, H_2	0.1–5
[10]	–	1.0	H, He^{2+}, Cl^{5+}	1, 3 MeV
[11]	–	–	H_2	0.1–5
[13]	–	–	Ti^{3+}	3–18
[14]	8	–	H	150
[15]	13	1.0	H, D, Ar, H_2, D_2, HD	0–5
[16]	5	0.76	H	20
[17]	–	–	Insulin, trypsin, human transferrin, β-galactosidase	10
[18]	–	–	He, heavy ions	∼MeV
[19]	–	–	Ions from atom probe	∼keV
[20]	8	1.0	Positron	3–30
[21]	–	–	He, C	60–140
[22]	15	0.85	Ne, Ar, Kr, Xe, H_2	0.5–4.5
	A_{open} = 0.63; L/D = 40:1; h = 0.5 or 2.0; front surface and channel contributions			
[23]	12	–	He, Ar, Xe	0.25,2, 5.4
[24]	–	0.9	O ($n = -1$, 0, 1)	0.03–1
[25]	–	–	Na, K	0.5–3
[26]	5	0.7	Multiply charged Ar	1.5–3
[27]	8	1.05	Recoil Nuclei, 3–16 u	300–8300
[28]	–	–	Insulin, tripsinogen, albumine ...	Velocity range 5–60 × 10^3 m s^{-1}
[29]	–	–	4–10 kDa biomolecules	5–20
[30]	11 (assumed)	0.9	H ($n = -1,0,1,2,3$), D, Ar	0.03–1
	A_{open} = 61%; L/D = 46:1; h = 0.5 (assumed); channel contribution only			

[a]The ions carry single positive charges ($n = 1$) unless otherwise stated. Only the paper of Gao et al. [3] reports measurements of $Q_i(\theta)$ at constant ion energy. As [9,19,27] deal with ion energies above 25 keV they are exceptional. Positron detection efficiencies reported in [20] are included for completeness.

An electron-accelerating potential difference V_o is established along the length of the channels. V_{coll} denotes the potential difference between a metal mesh of transparency T_m and the input surface of the first MCP in the (two- or three-plate) detector stack. If V_{coll} is positive, electrons released from the inter-channel web return to the plane of their emission, where they may enter a channel and contribute to the detection efficiency by initiating an electron avalanche. We write:

$$Q_i = T_m[Q_c + Q_s] \quad (2)$$

where the subscripts c and s denote, respectively, the contributions of the channels and of the MCP front surface.

This paper describes a general, predictive model of the MCP ion detection efficiency Q_i, based on previous accounts of electron [31] and soft X-ray [32,33] detection using MCPs and on simple expressions for the stopping power S and ion induced electron emission yield γ in planar solids [34–39]. The model, described in Sections 2 and 3 below, provides a framework for the interpretation of the diverse data sets referred to above and now summarised in Table 1. Section 4

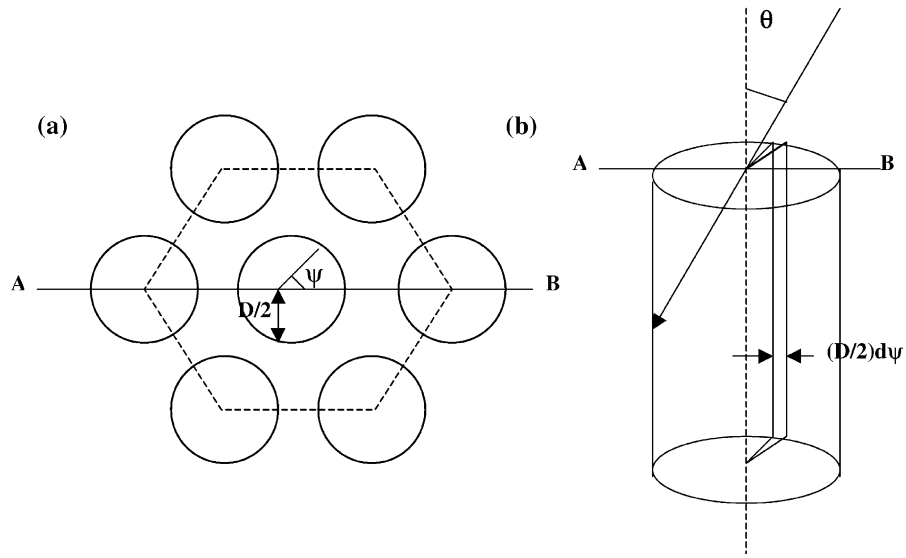

Fig. 1. (a) Unit cell of microchannel plate structure in plan view. A beam of ions is assumed incident from the right, travelling parallel to the axis AB. (b) Axial strip of channel wall, located at angular coordinate ψ. Angle of ion incidence θ indicated. The microchannel shown here has a bias angle of zero degrees.

reports some initial comparisons of the model with measurement and indicates the possible impact of alkali halide coatings on the sensitivity of future microchannel plate ion detectors, particularly those employed in time-of-flight analysis of large biomolecules.

2. Model

2.1. Ion-induced electron emission from a planar solid

A parallel, monoenergetic beam containing a single ion species is incident at grazing angle α to a homogenous planar solid, thickness T, whose vacuum interface lies in the plane $x = 0$. In the present context, the planar solid of interest is an infinitesimally narrow axial strip (see Fig. 1(b)) of MCP lead silicate glass, nickel—representing the electrode material—or alkali halide coating. Secondary electrons (with energies of a few eV) may be excited into vacuum by two processes: *kinetic emission*—arising from the direct transfer of the ion's kinetic energy—as described in the following section—and *potential emission*, described in Section 2.1.2. For ion velocities greater than $\sim 10^5\,\mathrm{m\,s^{-1}}$ (that is, for many practical detection problems involving light ions) kinetic emission dominates over potential emission [36].

2.1.1. Kinetic emission

The energy deposited by an ion in an element of path length dl, inclined at grazing angle α to the surface which is available for the creation of secondary electrons is given by:

$$\mathrm{d}E = BS_\mathrm{e}\mathrm{dl} \tag{3}$$

S_e is the electronic component of the stopping power and B ($0 < B < 1$) is the "near-far" partition factor originally introduced by Sternglass [35] and reviewed by Baragiola [36]. This factor, given the value of exactly one-half below, accounts for the equipartition of energy between the large-impact-parameter collisions responsible for the creation of low energy secondary electrons and "close" (i.e., unproductive) ion-atom collisions. If ε is the average energy required to produce a free electron in the solid, then the number

of free electrons created at depths between $(x, x + \mathrm{d}x)$ is:

$$N(x) = \frac{\mathrm{d}E(x)}{\varepsilon} = B\left\lfloor \frac{S_\mathrm{e}(x)}{\varepsilon}\,\mathrm{cosec}\,\alpha \right\rfloor \mathrm{d}x \tag{4}$$

The probability of one of those electrons escaping into vacuum is given by the usual semi-empirical formula:

$$P(x) = P(0)\exp\left(\frac{-x}{L_\mathrm{s}}\right) \tag{5}$$

where $P(0)$ is the probability of an electron at the surface actually escaping into vacuum and L_s is the secondary electron escape length. The kinetic component of the ion induced electron yield γ_k, is then found by integrating the product $N(x)P(x)$ over the thickness of the sample, giving:

$$\gamma_k = \frac{BP(0)\,\mathrm{cosec}\,\alpha}{\varepsilon}\int_0^T S_\mathrm{e}(x)\exp\left(\frac{-x}{L_\mathrm{s}}\right)\mathrm{d}x \tag{6}$$

The estimation of γ_k for any particular planar sample (such as a narrow element of microchannel wall parallel to the channel axis—Fig. 1(b)) therefore reduces to one of finding an appropriate expression for S_e and values for the parameters $P(0)$, L_s and ε. According to Beuhler and Friedman [34] the electronic component of the stopping power is given by:

$$S_\mathrm{e} = \left(\frac{8\pi^2 a_\mathrm{o}}{u_\mathrm{o}}\right)\xi F_\mathrm{e}(Z_\mathrm{i}, Z_\mathrm{t})v(x) = Av(x) \tag{7}$$

Furthermore, the *total* stopping power, determining the change in velocity v with x, the depth in the sample, is the sum of two components:

$$S = S_\mathrm{e} + S_\mathrm{n} = \left\lfloor \frac{\mathrm{d}E}{\mathrm{d}x} \right\rfloor_\mathrm{e} + \left\lfloor \frac{\mathrm{d}E}{\mathrm{d}x} \right\rfloor_\mathrm{n} \tag{8}$$

where S_n is the nuclear stopping power:

$$S_\mathrm{n} = \left(\frac{\pi^2 e^2 a_\mathrm{o}}{2.718390}\right)\left\lfloor \frac{M_\mathrm{i}}{M_\mathrm{i} + M_\mathrm{t}} \right\rfloor F_\mathrm{n} s(E_\mathrm{i}') \tag{9}$$

and F_e, F_n are the subsidiary functions

$$F_\mathrm{e}(Z_\mathrm{i}, Z_\mathrm{t}) = \frac{1}{4\pi\varepsilon_\mathrm{o}} N_\mathrm{o}\left\lfloor \frac{Z_\mathrm{i}Z_\mathrm{t}}{(Z_\mathrm{i}^{2/3} + Z_\mathrm{t}^{2/3})^{3/2}} \right\rfloor \tag{10}$$

and

$$F_\mathrm{n}(Z_\mathrm{i}, Z_\mathrm{t}) = [Z_\mathrm{i}^{2/3} + Z_\mathrm{t}^{2/3}]F_\mathrm{e}(Z_\mathrm{i}, Z_\mathrm{t}) \tag{11}$$

Table 2
Parameters in the stopping power formulae, Eqs. (7)–(11).

Symbol	Meaning	Numerical value
a_o	Bohr radius	0.53 Å
u_o	Bohr velocity	$2.2 \times 10^6\,\mathrm{m\,s^{-1}}$
Z_i	Atomic number of incident ion	Variable
Z_t	Effective atomic number of target	MCP lead glass: 11.24 [33] Ni: 28 NaCl: 14.64 CsI: 54.02
M_i	Atomic mass of incident ion (u)	Variable
M_t	Effective mass number of target (u)	MCP lead glass: 22.47 [33] Ni: 58.69 NaCl: 30.56 CsI: 130.1
ξ	Dimensionless parameter	Equal to $Z_\mathrm{i}^{1/6}$: for empirical adjustments, see text.
N_o	Number density of target atoms	MCP glass: $8.84 \times 10^{28}\,\mathrm{m^{-3}}$ Ni: $9.11 \times 10^{28}\,\mathrm{m^{-3}}$ NaCl: $4.25 \times 10^{28}\,\mathrm{m^{-3}}$ CsI: $2.1 \times 10^{28}\,\mathrm{m^{-3}}$

The scaling factor $s(E_i')$ is a piecewise function of the so-called reduced ion energy, originally introduced by Lindhard and Schaff [37] and developed by Schou [38] and by Holmen et al. [39].

The parameters appearing in Eqs. (7)–(11), together with their numerical values appropriate to microchannel plate materials, are identified in Table 2. The electron charge and the permittivity of free space are represented by the usual symbols.

To calculate γ_k exactly requires a stepwise approach, starting with the velocity of the ion at entry into the surface, calculating first the stopping power for that velocity and then the velocity at a new position, an incremental distance dl along the ion's trajectory. Fortunately, one can use the low-velocity approximation (see Fig. 2 [34]) that:

$$S_n > S_e$$

in order to arrive at a closed, analytical approximation to γ_k. Given that S_n is independent of velocity and assuming that, for the purposes of estimating the velocity correction, the ions are incident normally to the surface:

$$v(x) = \left(\frac{2}{M_i}\right)^{1/2} (E - xS_n)^{1/2} \tag{12}$$

Substituting Eq. (12) in Eq. (6) produces an integral of a transcendental function which has no simple analytical solution. Expanding the exponential term as a power series, however, and ignoring terms of order higher than x leads, after some manipulation, to the final result:

$$\gamma_k = \left(\frac{ABP(0)\,\mathrm{cosec}\,\alpha}{\varepsilon}\right) vL_s \left[1 - \left(\frac{L_s}{2x_{max}}\right) - \frac{1}{2}\left(1 - \left(\frac{L_s}{x_{max}}\right)\right) \exp\left(-\frac{x_{max}}{L_s}\right)\right] \tag{13}$$

where v denotes the ion velocity in free space and:

$$x_{max} = \mathrm{Min}\left(\frac{E}{S_n}, T\right) \tag{14}$$

Inspection of Eq. (13) reveals an ion induced electron yield depending explicitly, not on the ion energy E, but on the ion velocity v. The MCP ion detection efficiency (expressed in counts/incident ion) found by integrating the contributions of axial strips of channel wall (Fig. 1(b)), is also likely to be determined by velocity, in keeping with the experimental conclusions of Twerenbold et al. [28], working with large protein ions (see Section 4.2). This scaling law is important for the developing field of biomolecule identification by mass spectrometry [17,28,29].

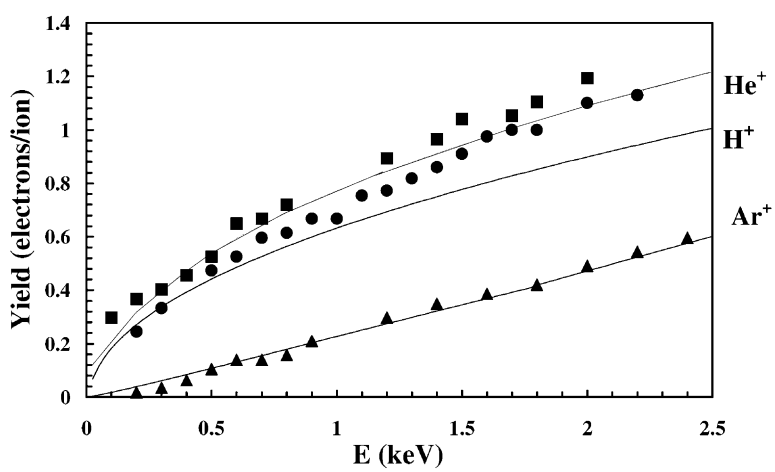

Fig. 2. Comparison of measured (individual symbols) and calculated (full curves) ion induced electron yields for singly-charged H, He and Ar incident on no. 46 glass [45]. Normal incidence. Triangles: argon ions; circles: atomic hydrogen and squares: helium.

Table 3
First and second ionisation potentials for named ions [40]

	H	H_2	He	O	O_2	N	N_2	Ne	Ar	Kr	Xe
First ionisation potential (eV)	13.6	15.4	24.48	13.61	12.5	14.53	15.8	21.56	15.76	14.0	12.13
Second ionisation potential (eV)	–	–	54.4	35.11	–	29.59	–	41.07	27.62	24.56	21.2

2.1.2. Potential emission

If E_f, the ground-state neutralisation energy (the first ionisation potential for singly charged ions, the sum of the first and second ionisation potentials for doubly charged ions) is greater than about twice ϕ, the work function/band gap of the target solid, then the potential energy released by neutralisation of the incident ion can provide the energy necessary to free electrons from that solid. There are three features of this component of the ion induced electron yield, γ_p:

(i) γ_p is energy independent (and therefore must dominate over the kinetic component (above) at sufficiently low ion velocities).
(ii) For ion/solid combinations for which $E_f < 2\phi$, the potential component of the yield is zero.
(iii) Potential emission, unlike kinetic emission, contains a dependence on the charge state of the ion through the ground state neutralisation energy.

According to Baragiola et al. [36] the potential yield (strictly speaking, for noble gas ions incident on polycrystalline metal surfaces) is given empirically by:

$$\gamma_p = 0.032[0.78E_f - 2\phi] \quad (15)$$

where E_f and ϕ are in eV. Table 3 gives ionisation potential values for a number of common ions [40].

2.1.3. Electron yields for molecular ions and negatively charged ions

The electron yield $\gamma = \gamma_k + \gamma_p$ resulting from the impact of a (light) molecular ion is less than or equal to the sum of the yields for each molecular component *at the same velocity* [36]. Thus, for a diatomic ion X_2^+:

$$\gamma(X_2^+, v) \leq 2\gamma(X^+, v) \quad (16)$$

There is much current interest in establishing the upper mass limit of applicability of this *addition rule*. The addition rule may also be used to estimate the yield due to neutrals and negatively charged ions [41]. For example, for the hydrogen ion series H^-, H^0, H^+ ($n = -1, 0, +1$):

$$\gamma(H^0) = \gamma(H^+) + \delta_e \quad (17a)$$

$$\gamma(H^-) = \gamma(H^0) + \delta_e = \gamma(H^+) + 2\delta_e \quad (17b)$$

Here δ_e denotes the secondary electron yield for an incident primary electron moving at the common incident velocity. Because the electron mass is much lower than any ion mass ($M_e/M_p = 1/1824$), this term is transposed to very low electron energies and so may be neglected. Thus, to first order, we expect the ion induced electron yield for negatively charged and neutral hydrogen to be the same as for H^+. However, the non-zero probability of elastic electron backscatter (Hill [42] estimates a probability $\sigma \sim 0.05$ for 300 eV electrons normally incident to MCP lead glass) must also be taken into account. Thus, for low ion energies (i.e., when $\gamma(E) < 1$), the addition rule indicates that the MCP detection efficiency for a negatively charged ion should exceed that for the same species positively charged.

The formulae presented in Sections 2.1.1–2.1.3 provide a framework for the calculation of ion yield γ as a function of the ion's nuclear charge, mass, energy and electronic charge. Specifically:

(i) Eqs. (16)–(17) allow us to begin to estimate the yields due to molecular ions.
(ii) Eq. (15), describing potential emission, brings in a dependence on electronic charge state.
(iii) Eqs. (7)–(14) account for Z_i and M_i and the properties of the emitting surface.

In the next section, we account for the cylindrical geometry, surface composition and electrostatics of a

working microchannel plate, finally arriving at expressions for the MCP ion detection efficiency.

2.2. MCP ion detection efficiency

2.2.1. Channel contribution Q_c

Adapting Eq. (3) of [31], we may write, for a uniform cylindrical channel whose long axis is perpendicular to the MCP input surface (i.e., for which the bias angle $\theta_B = 0^\circ$):

$$Q_c = \frac{4}{\pi} A_{open} \int_0^{\pi/2} [1 - R(\alpha)] \cdot f(\theta_t) \cdot \cos^2 \psi \cdot \left\{1 - \exp\left[-\gamma(E, \alpha) \cdot \delta_e\left(E_e, \frac{\pi}{2}\right)\right]\right\} \cdot d\psi \tag{18}$$

where ψ is the channel azimuth angle (Fig. 1(a)), related to the grazing angle α and incident angle θ (Fig. 1(b)) by:

$$\sin\alpha = \sin\theta \cos\psi \tag{19}$$

The term $f(\theta_t)$ accounts for the geometric transparency of the channel. For angles less than the transparency angle, $\cot^{-1}(L/D)$, radiation may pass through the plate without striking the channel walls. δ_e is the secondary electron yield of MCP glass [42]. E_e is the energy with which low energy electrons liberated by the initial ion impact next strike the channel wall. From a two-dimensional approximation to electron trajectories [31]:

$$E_e = \frac{eV_o^2}{4U(L/D)^2} \tag{20}$$

where L, D and V_o have the meanings assigned in Section 1 and eU is the mean emission energy ($U \sim 3.1$ V [31,42] for MCP glass and 3.5 V for nickel [31]) of the secondary electrons released into vacuum by the ion impact.

$R(\alpha)$ is the probability of ion reflection from the channel surface. Eq. (18) assumes that any ion undergoing grazing incidence reflection from the channel wall is "lost" whereas in the corresponding X-ray analysis [33], an attempt was made to account for multiple reflections. The difference is that, in the X-ray case, the Fresnel equations provide a straightforward analytical means of estimating channel reflectivity. The backscattering of light ions is a rather more complex problem [43]. Using the Rutherford scattering cross-section [44], one may obtain some limited approximations for the reflectivity but, in what follows, we have chosen to represent R by the simple empirical relationships:

$$R = R_o : \ \alpha < \alpha_{crit} \tag{21a}$$

$$R = 0 : \ \alpha > \alpha_{crit} \tag{21b}$$

where the critical angle and ion energy are linked by the equation:

$$E\,\alpha_{crit} = C_o \tag{22}$$

and the ion-species-independent parameters R_o ($0 < R_o < 1$) and C_o are determined by fitting to measured efficiency-versus-angle data (Section 4.1). A non-unity value for R_o implies the presence of significant surface roughness.

In every real channel plate, the channel composition varies with depth down the channel. Nickel-based electroding (or an evaporated alkali halide layer) accounts for the first h channel diameters and MCP glass for the rest. We account for this dual composition by calculating the channel efficiency twice, once for the electrode/coating material and once for the channel glass. We then weight the results by the probabilities of the ions striking the two materials, to obtain:

$$Q_c = (h \tan\theta) Q_c^{electrode} + (1 - h \tan\theta) Q_c^{glass} \tag{23}$$

2.2.2. Front surface contribution

Again following [31], we may write:

$$Q_s = (1 - A_{open})[1 - (1 - p_a p_l)^{\gamma(E, \pi/2 - \theta)}] \tag{24}$$

Here, p_l is the mean lensing probability—the probability that an electron released from the inter-channel web is returned to the plane of its emission by the electric field established between the front surface of the input MCP and the mesh. The lensing probability can be calculated numerically as a function of V_{coll}, p and D [33]. In what follows, we shall assign it its maximum geometric value, $p_l = A_{open}$. Next, p_a is the

probability that the re-entrant electron releases a secondary electron from the channel wall and so initiates an avalanche. The minimum value of p_a, appropriate to electrons striking the channel rim and thus gaining no energy from the channel bias field, is:

$$p_a = 1 - \exp(-(eU)) \quad (25)$$

where δ and eU, in a bare MCP, are, respectively, the secondary yield coefficient of the channel wall at the point of electron impact and the mean emission energy of the nickel-based electrode material.

3. Determination of material parameters

3.1. Lead silicate glass

Most of the material parameters required for the ion analysis have already been identified [31–33]. In addition to the parameter values given in Table 2, the key secondary electron escape parameters for MCP glass are already known:

$$P(0) = 0.15, \qquad L_s = 33\,\text{Å}, \qquad \varepsilon = 10\,\text{eV}$$

In order to calibrate our model, we first need experimental ion induced electron yields from planar, macroscopic samples of MCP glass. The closest (indeed only) approximation to this data set is to be found in the paper by Batanov [45]. Batanov's glass, identified only by a type number (no. 46), was bombarded at normal incidence by (atomic and molecular) hydrogen, helium and argon ions with energies between 0.1 and 30 keV. The resulting electron yields are compared with the present model in Figs. 2–4. Yields for helium and argon were computed using a common ξ value of 1.3, rather than the values of 1.12 and 1.62 dictated by the $Z^{1/6}$ rule given in Table 2. Accepting this element of fitting, the agreement between theory and experiment is reasonably good, especially given our ignorance of the detailed glass composition and the reported dependence of the yield on target state [45]. The simplest form of the addition rule for molecular ions (setting both sides of Eq. (16) equal) appears to overestimate the yield differences for singly-charged H, H_2 and H_3 ions at low energies (see Fig. 3), but produces a very good fit to the H_2-induced yield at higher energies (see Fig. 4). As noted by Batanov, the yield-versus-energy curve for He does not tend to zero at zero energy, indicating a contribution from potential emission. Following [45] and adopting $\phi = 8\,\text{eV}$, Eq. (15) and Table 3 lead us to a γ_p value of 0.1 electrons/ion, a value incorporated in the theoretical curves for He shown in Figs. 2 and 4.

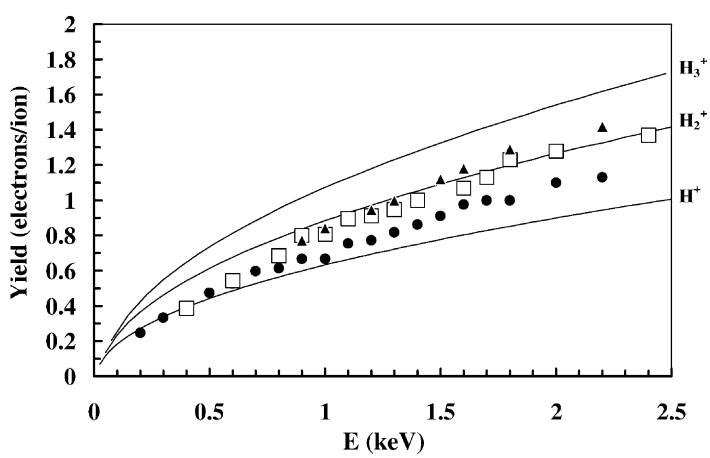

Fig. 3. Comparison of measured (individual symbols) and calculated (full curves) ion induced electron yields for singly charged H, H_2 and H_3 incident on no. 46 glass [45]. Normal incidence. Circles: atomic hydrogen; squares: H_2 and triangles: H_3.

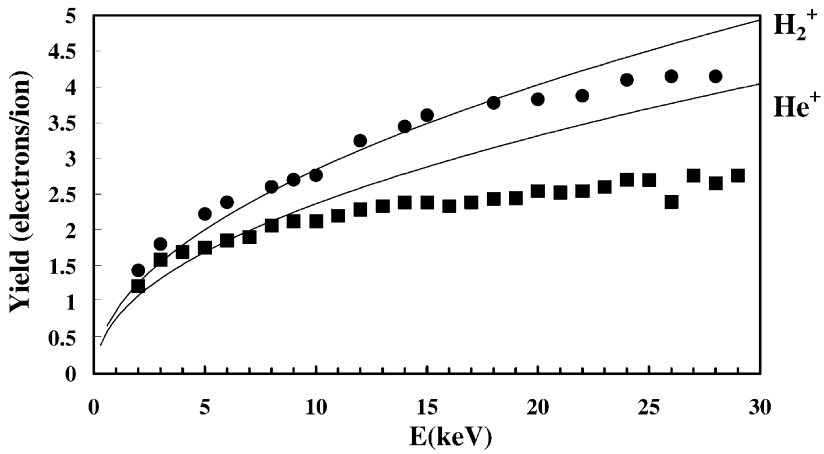

Fig. 4. Comparison of measured (individual symbols) and calculated (full curves) ion induced electron yields for singly charged He and H_2 incident on no. 46 glass [45]. Normal incidence, extended energy range. Squares: helium and circles: H_2.

3.2. Electrodes

We have used the data of Cawthron [46] for the ion bombardment of nickel at 45° incidence to investigate the quality of the model in the case of nickel-based electrode materials. Here, the secondary electron escape parameters are not known a priori; the results shown in Fig. 5 were obtained with [47]:

$$P(0) = 0.06, \qquad L_s = 20\,\text{Å}, \qquad \varepsilon = 6.65\,\text{eV}$$

and with a ξ value of 1.3 for all ions except hydrogen. The small values of $P(0)$ and L_s are typical of metals, while the value of the third parameter reflects the Ni bandgap. The calculated yields for He and Ne contain potential energy emission contributions of 0.176 and 0.103 electrons/ion, respectively. The general trends of the data are reproduced by the calculations; the variable quality of the fits—excellent for hydrogen, less good for argon—may in some way reflect the extreme experimental conditions [46] (target heated "red hot"). We note that the early data of Higatsberger et al. [48] implies much higher yields for 2–6 keV argon ions ($\gamma = 3.8$ at 5.5 keV) incident on nichrome at 45°.

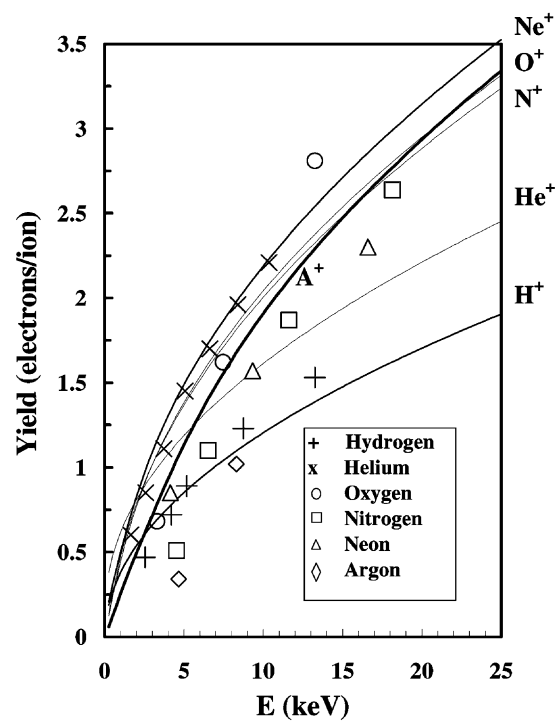

Fig. 5. Comparison of measured (individual symbols) and calculated (full curves) ion induced electron yields for singly charged H, He, O, N, Ne and Ar incident at 45° to nickel [46]. The calculated curve for argon is shown bold for clarity.

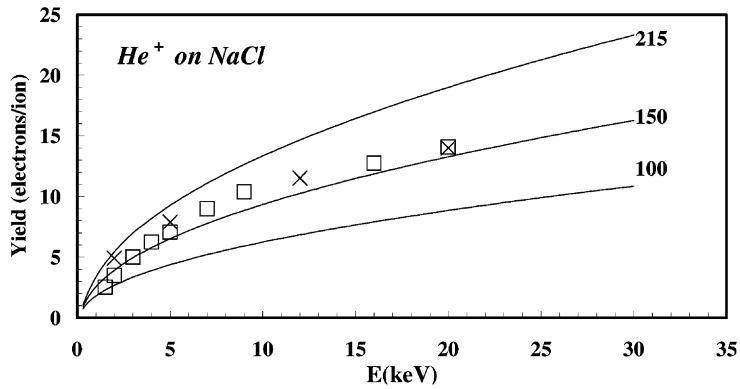

Fig. 6. Comparison of measured (individual symbols) and calculated (full curves) ion induced electron yields for singly charged helium ions normally incident on NaCl. The three model curves correspond to L_s values of 215, 150 and 100 Å. Crosses: 20 °C data from Baboux et al. [50] and squares: Konig et al. [51] data.

3.3. Alkali halides

MCP coating with alkali halides to increase the soft X-ray detection efficiency detectors is a well-known process, but the technique has not been generally adopted in ion detection, possibly because there has been to date no comprehensive study, either experimental or theoretical, of the efficiency enhancements which might be expected. Now, with the required secondary electron escape parameters already determined by analysis of X-ray data [49] and the availability of ion-induced electron yield data from a number of alkali halides—NaCl, KBr, KCl, LiF and CsI [50–53] and from MCP lead silicate glass, we are in a position to begin such a systematic analysis.

First, Figs. 6 and 7 examine the case of NaCl for which the X-ray analysis indicates [49]:

$$P(0) = 0.24, \qquad L_s = 215\,\text{Å}, \qquad \varepsilon = 9\,\text{eV}$$

Fig. 6 shows model $\gamma(E)$ curves for He^+ on NaCl, calculated for secondary electron escape lengths of 215 (the X-ray baseline), 150 and 100 Å. The best fit to the measurements [50,51] is given by the intermediate value of escape length. Comparing Fig. 6 with Fig. 3, we see immediately that the alkali halide, by virtue of its much increased secondary electron escape length, confers an asymptotic yield enhancement for He^+ of ∼5 times at energies above about 20 keV. The potential contribution to the yield for He^+ on NaCl is negligible −0.035 electrons/ion.

Fig. 7 compares measured [51] and calculated normal incident yields for singly charged He, Ne, Ar, Kr and Xe incident on NaCl, with L_s fixed at 150 Å. The quality of agreement varies from ion species to ion species—excellent for He^+, poor for Ne^+—but the model generally confirms that high yields can be expected over a wide range of ion masses.

The MCP photocathode of choice for X-ray detection is CsI. Little ion yield data, however, is available for this material. Moshammer and Matthaus [52] re-

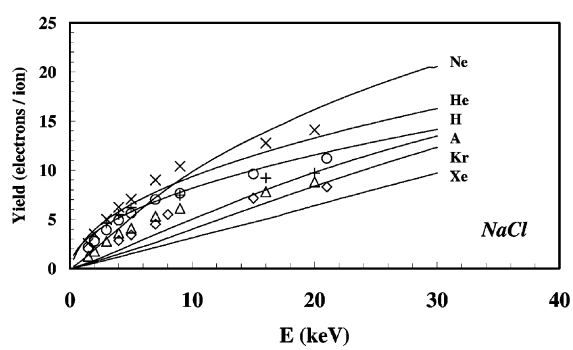

Fig. 7. Comparison of measured [51] (individual symbols) and calculated (full curves) ion induced electron yields for singly charged H; He (×); Ne (+); Ar (○); Kr (triangles) and Xe (diamonds) normally incident on NaCl. Normal incidence. Calculations assume $L_s = 150$ Å.

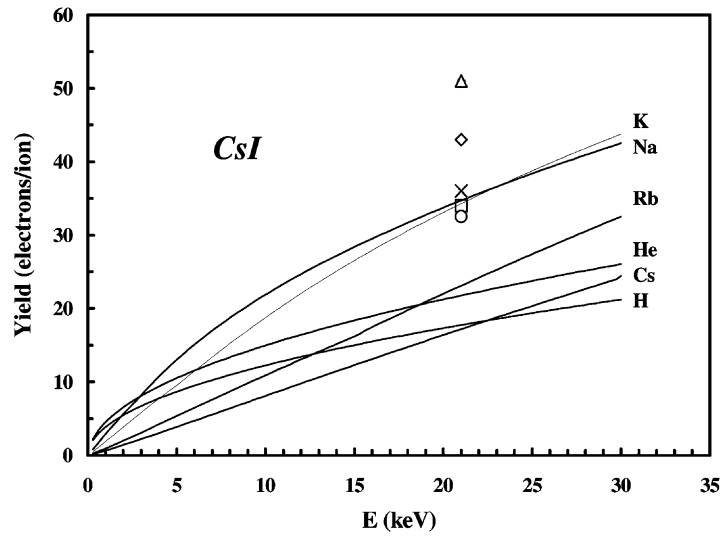

Fig. 8. Calculated yield-versus-energy curves for named singly charged ion species normally incident upon CsI. Calculations assume $P(0) = 0.35$. Individual symbols—measured 21 keV yields from [52]: H (square); Na (diamond); K (triangle); Rb (circle); Cs (cross).

port yield-versus-mass measurements at a fixed ion energy of 21 keV for both singly-charged monatomic (H, Na, K, Rb and Cs) and molecular ions (masses up to 200 u, plus Gramecidine at 1882 u). Figs. 8 and 9 compare this data with calculations based on the CsI X-ray parameter set [49]:

$$P(0) = 0.35, \qquad L_s = 215\,\text{Å}, \qquad \varepsilon = 7\,\text{eV}$$

Fig. 8 shows the yield-versus-energy curves for CsI computed on this basis. Agreement between theory

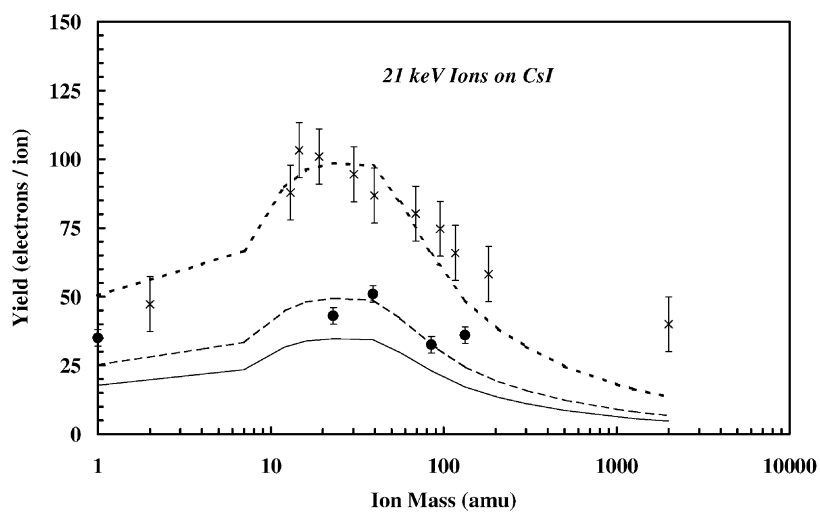

Fig. 9. Calculated ion-induced electron yield-versus-mass curves for CsI. Normal incidence, ion energy fixed at 21 keV. Bottom curve $P(0) = 0.35$; middle curve $P(0) = 0.5$; top curve $P(0) = 1.0$. Individual symbols—comparable data from [52]. Squares: singly charged monatomic H, Na, K,Rb and Cs and crosses: molecular ions (glycine, valine ...).

and experiment is reasonable at the fixed energy of 21 keV [52], except in the case of hydrogen. The situation becomes a little clearer when the same data is plotted versus ion mass, as shown in Fig. 9. For monatomic ions, the electron yield peaks, experimentally and theoretically, between about 20 and 40 u, while a scaling-up from $P(0) = 0.35$ to $P(0) = 0.5$ brings theory and measurement into quite close agreement. The theoretical curves are based on individual calculations for singly-charged H, He, Li, C, O, Fe, Nb and Pb and, for masses greater than 207 u, for pseudo-ions with atomic numbers equal to one-half their mass numbers. Summarising their heavy molecular ion measurement, Mosshamer and Matthaus [52] state that (a) the addition rule (see Eqs. (17a) and (17b)) does not apply and (b) the ion induced electron yields are very nearly independent of molecular structure and composition. That is, the yield-versus-mass curve at fixed ion energy is a *universal* curve, which Fig. 9 shows is closely approximated (at least up to 200 u) by the function which results from simply scaling our calculated monatomic ion yields to $P(0) = 1.0$. Thus, by assuming that every electron produced by a simple ion of a given mass escapes into vacuum, we can simply estimate the electron yield of an arbitrarily complex molecular ion of that same mass. At the highest mass in the Mosshamer and Matthaus [52] data set (Gramecidine), the discrepancy is just greater than a factor of two. The results of Westmacott et al. [17] indicate an electron yield-to-projectile mass ratio of 1.5×10^{-4} for an energy per unit mass of 2 eV/u. This translates to a yield of 1.58 electrons/ion for a 21 keV, 10,500 u molecular ion—broadly in line with a continuation of the $P(0) = 1$ model curve in Fig. 9. As reported by Van Tan Nyugen and Wien [53], the response of CsI layers to heavy molecular ions is quite sensitive to surface conditioning.

4. Comparison of measured and calculated Q_i

4.1. Gao et al. data

The efficiency-versus-energy measurements of Gao et al. [3] are a key data set because (uniquely) they are coupled to measurements of the relative efficiency-versus-angle, so providing a basis for the determination of the only remaining unconstrained model parameters, R_o and C_o. Table 1 lists the MCP parameters from Gao et al. (and from the experiments analysed in Sections 4.2–4.4 below) which are required inputs for our efficiency calculations.

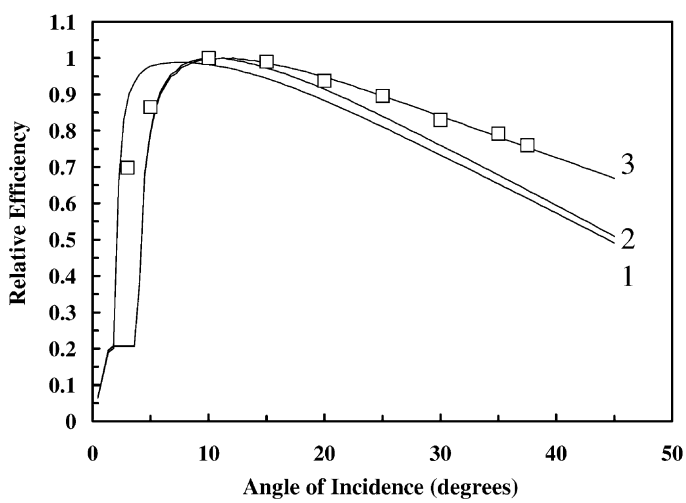

Fig. 10. Comparison of measured (squares [3]) and calculated (full curves) relative efficiency-versus-angle functions. Angle of incidence measured relative to channel axis. See text for details of Curves 1–3.

Fig. 10 compares the relative efficiency-versus-angle function given in Fig. 7 [3], representing an average of data obtained with 750–3000 eV H, He and Ne ions, with three different model curves, all computed for 1 keV H^+ ions. Curve 1 assumes that the electrode penetration depth is one channel diameter, that $R_o = 0.8$ and that the critical angle of reflection is 2° at 1 keV. Curve 2 retains the same values of R_o and h, but adopts a critical angle value of 4° at 1 keV. Curve 3—which provides a satisfactory fit to the data—is based on the same assumptions as Curve 2, except that the effective electrode penetration depth is set to one-half times the channel diameter. In Fig. 11, we adopt this best fit parameter set to account for the $Q_c(E)$ data for singly charged H, He and O ions reported in [3]. The model correctly reproduces the ion efficiency "ranking" (H > He > O) and the "saturation" of the channel efficiency at the open area fraction (55%) but the inadequacy of the simple reflectivity model is also apparent for "low" energies.

4.2. Oberheide et al. data

Measurements of the absolute total efficiency (i.e., front surface contribution plus channel contribution, with the mesh transmission T_m factored out) for singly-charged noble gas ions and for molecular hydrogen are reported in [22]. In addition, the paper considers the influence of electrode penetration, reporting a significant reduction in efficiency when h is increased from 0.5 to 2.0 channel diameters. Table 1 summarises the relevant experimental parameters; the numerical description of the ion reflectivity function is carried forward from Section 4.1.

Fig. 12 compares the measured efficiency-versus-energy curve for Ne^+ with the model curves. We find that the data is rather well described by a model in which (Section 2.2.2) the probability p_a has its minimum value. Fig. 13 shows that fits of similar quality are then obtained for singly-charged argon, krypton and xenon. Use of the addition rule (Eq. (16)) accounts for the molecular hydrogen data [22], successfully predicting, as shown in Fig. 14, a lower "saturation" energy and a lower efficiency "plateau" than for the noble gas ions. Fig. 15, finally, shows that the model can account for the reduction in asymptotic efficiency (from $63.5 \pm 1.5\%$ to about 45%) observed when the former exit face of the MCP—with electrode penetration characterised by $h = 2$ rather than 0.5—is exposed to the ion beam. To reproduce the observed

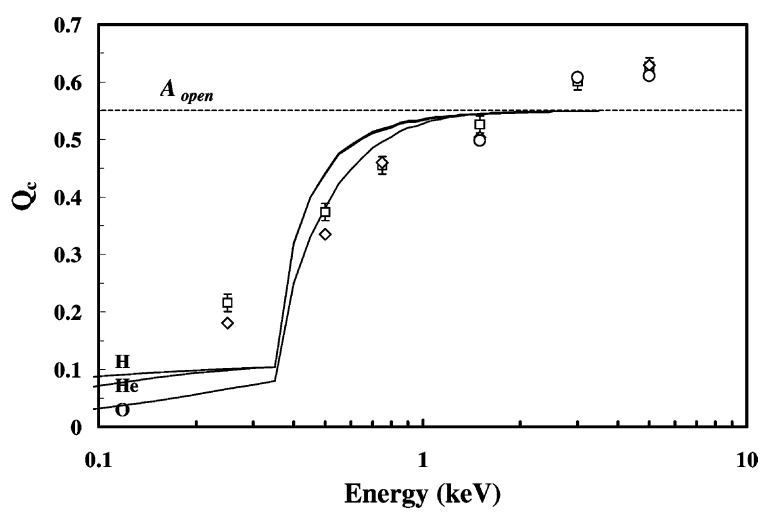

Fig. 11. Comparison of measured (individual symbols [3]) and calculated (full curves) variation of open area efficiency with ion energy. Angle of incidence: 11° (i.e., normal ion incidence to an MCP with 11° bias angle). Circles: O^+; diamonds: He^+; squares: H^+; MCP open area fraction indicated by broken horizontal line.

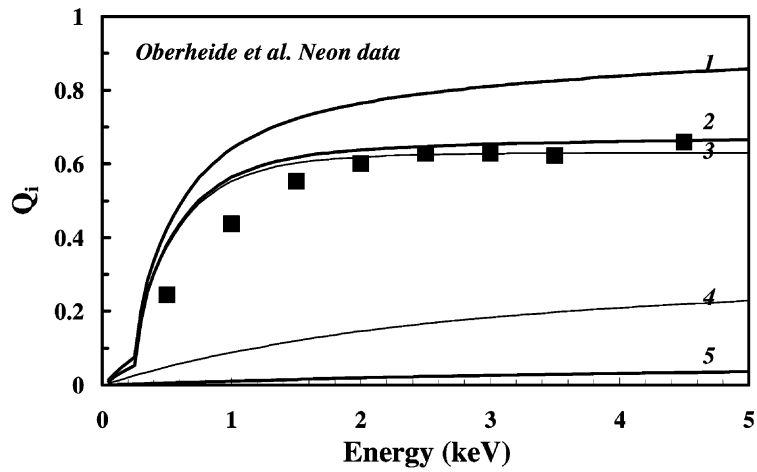

Fig. 12. Comparison of measured (squares) and calculated ion detection efficiencies for singly-charged neon [22]. Theoretical curves: 1 is the upper limit to the total efficiency based on $p_l = A_{open}$, $p_a = 1$. 2 is the lower limit to the total efficiency using $p_l = A_{open}$, minimum value of p_a based on null acceleration of electrons re-entering the front surface, $U = 3.5$ V and a first crossover potential for MCP glass of 20 eV. 3 is the open area efficiency Q_c. 4 is the upper limit to front surface efficiency Q_s and 5 is the lower limit to Q_s.

fall in "saturated" efficiency requires the assumption that the electrons again strike the electrode material when they enter a microchannel.

4.3. Peko and Stephen data

The experimental study reported in [30] is among the most comprehensive to date, providing (albeit with fairly large uncertainties—10–20% depending on the ion species and energy) information on the differences in MCP detection efficiency between (a) positively charged, neutral and negatively charged ions and (b) between hydrogen and deuterium ions of the same energy.

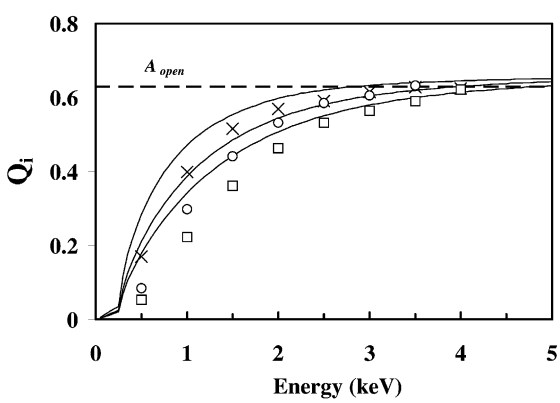

Fig. 13. Comparison of measured (individual symbols) and calculated ion detection efficiencies [22]. Crosses and uppermost curve: singly charged argon; circles and middle curve: singly charged krypton; squares and bottom curve: singly charged xenon; MCP open area fraction indicated by broken horizontal line.

All the results presented in [30] are in a "low energy, small angle" regime (sub-keV energies and we assume normal incidence to an MCP with 11° bias angle) where ion reflection is highly significant and where the present model will therefore have limited success. Nevertheless, Fig. 16 shows that we are able to reproduce the ordering of efficiencies for singly charged hydrogen, oxygen and argon down to energies of only 50 eV. The predicted efficiencies for Ar^+ are, however, much higher than measured.

Fig. 17 shows that the model also reproduces the "isotope effect" reported in [30], whereby efficiencies for H^+ are found to be systematically higher than for D^+. Fig. 18, finally, shows that the superior low energy efficiencies measured for H^- and H^0 can be partially accounted for the inclusion in the model of an electron elastic backscatter probability of 5% (see Eqs. (17a) and (17b) and Section 2.1.3). We note that the very high efficiencies measured for H^- ions at en-

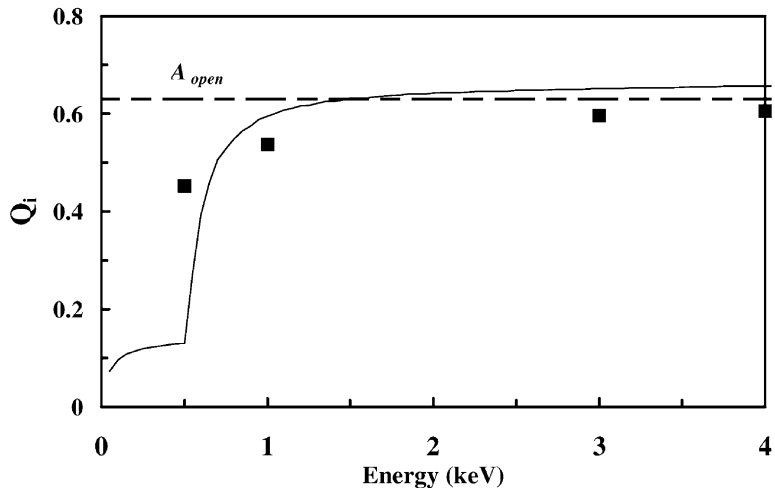

Fig. 14. As Fig. 13, except the ion species is singly-charged H_2 [22]. MCP open area fraction indicated by broken horizontal line.

ergies below 400 eV may have an origin in the field configuration at the input surface of the detector [30].

4.4. Twerenbold et al. data

There is much current interest in understanding the response of MCPs to large, slow-moving biomolecules of up to 500 kDa (1 Dalton (Da) = 1 atomic mass unit (u)). As described in the review by Frank [54], microchannel plates, based on secondary electron emission, are being challenged in fields such as proteomics [28] by cryogenic detectors whose sensitivity does not decrease with increasing mass. Twerenbold et al. [28] have recently reported a "universal"

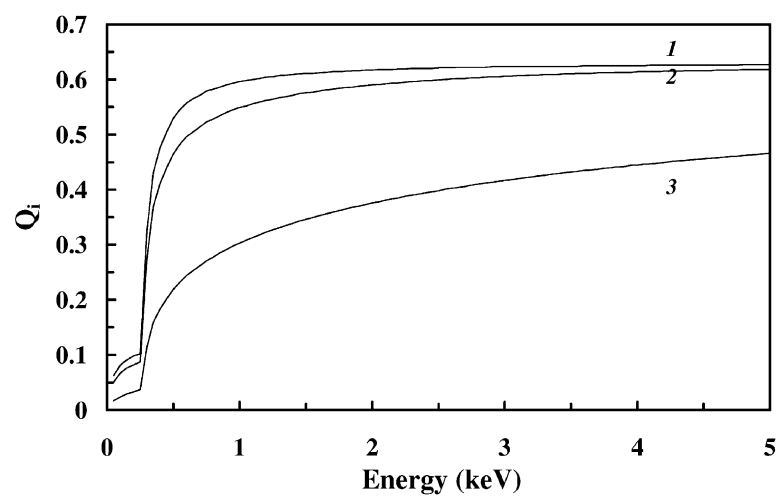

Fig. 15. Total efficiency vs. ion energy calculations for the experimental geometry of Oberheide et al. [22]. All curves computed for H^+ ions. Curve 1: electrode penetration $h = 0.5$. Curve 2: $h = 2.0$, electrons liberated from MCP front surface assumed to make first collision (with no gain in energy) with lead glass component of the channel wall (first crossover potential, 20 V). Curve 3: as curve 2, except collision assumed to be with electrode material (first crossover potential taken to be 100 V).

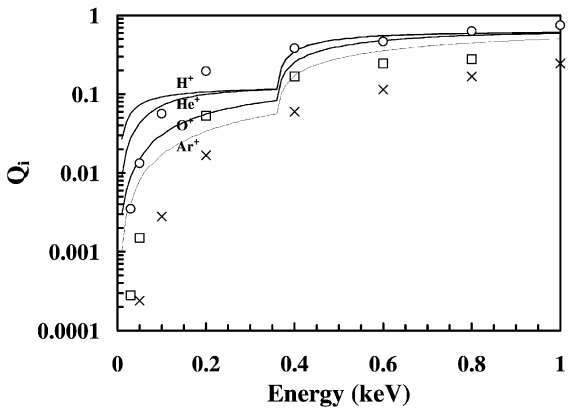

Fig. 16. Comparison of measured (individual symbols) and calculated (full curves) ion detection efficiencies for the detector geometry of Peko and Stephen [3]. Circles: H^+; squares: O^+; crosses: Ar^+. An additional model curve for singly charged helium is shown for completeness.

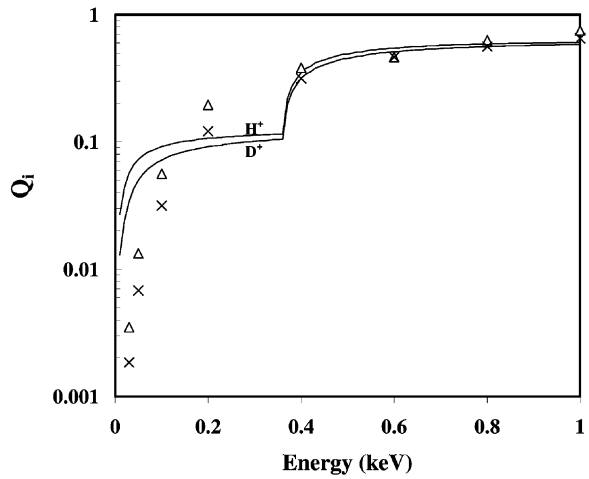

Fig. 17. Comparison of measured (individual symbols [30]) and calculated (labelled curves) ion detection efficiencies for singly charged hydrogen and singly charged deuterium. Triangles: H^+; crosses: D^+.

(i.e., species-independent) curve for the high-mass detection efficiency of microchannel plates relative to the (assumed) unit efficiency of a superconducting tunnel junction (STJ) detector. Expressing the ion kinetic energy E in units of keV and the ion mass M_i in atomic mass units, the empirical relationship is:

$$Q_c = A_{open}[1 - \exp(-1620(E/M)^{1.75})] \quad (26)$$

This curve, evaluated for $E = 16$ keV [55] and masses up to 100 kDa, is represented by the squares in Fig. 19. The extension of the present model to the large mass regime is not straightforward, but must take into account:

(a) The fact that a fraction (between 25 and 50% [54]) of the ion energy is lost on impact with the

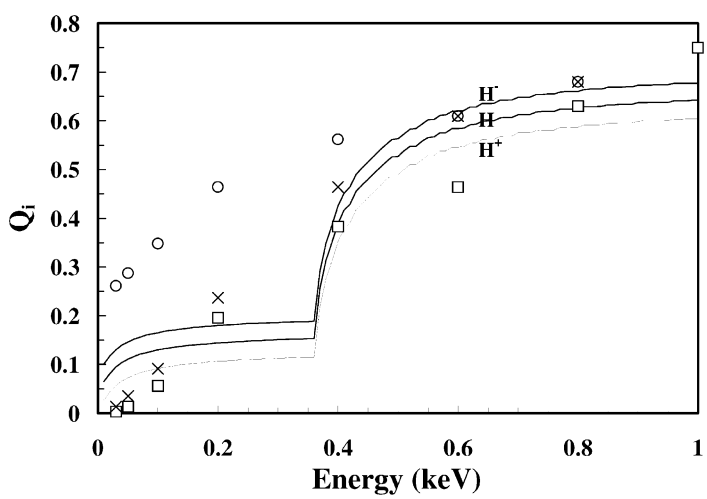

Fig. 18. Comparison of measured (individual symbols [30]) and calculated (labelled curves) ion detection efficiencies for H^-, H^0, H^+. Circles: negatively charged atomic hydrogen; crosses: neutral atomic hydrogen; squares: positively charged atomic hydrogen.

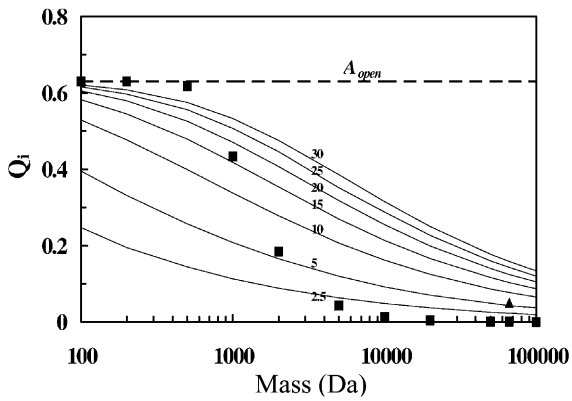

Fig. 19. Calculated variation with mass of the channel efficiency of an MCP of the Oberheide et al. geometry [22]. Individual curves labelled with ion energies in keV. Open area fraction indicated by the broken horizontal line. Squares: experimental fit to macromolecular ion relative efficiency data of Twerenbold et al. [28]; triangle: data point (5% at 30 keV acceleration for a 66,400 u bovine albumine ion) from Frank et al. [54].

detector as a result of bond breaking, deformation of the molecule and the ejection of molecular fragments. This fraction is dependent on ion type.

(b) The likely modification of the secondary electron yield of the multiplier by coating with these fragments.

(c) The likely breakdown of the cosec α dependence of the ion induced electron yield for the surface interaction of non-penetrating large ions.

We have attempted to address point (c) in producing the model curves of Fig. 19. All seven curves, representing ion energies between 2.5 and 30 keV, have been calculated with the ion induced electron yield everywhere set equal to its normal incidence value. We see that the efficiencies predicted by Eq. (26) do not conform to a single model curve, i.e., do not correspond to a constant value of ion energy. With $E =$ 16 keV and fractional energy losses on impact of up to 50%, one would expect the squares representing Eq. (26) to lie close to the curve computed for 10 keV effective ion energy. Fig. 19 also includes an efficiency value cited by Frank [54]: 5% for 66.4 kDa ions accelerated to 30 keV. As acknowledged in [28,55], data from the Lawrence Livermore group lies up to one order higher in efficiency than the values given by "universal" function expressed here in Eq. (26) and may reflect a real difference in MCP operating conditions.

5. Discussion

A comprehensive model of the ion detection efficiency of microchannel plates has been shown to account for a wide range of measurements in which the experimental variable is ion energy, species or angle of incidence. The model may therefore be immediately useful in computing the influence of the channel aspect ratio L/D and the MCP bias voltage [23] on the channel component of the efficiency Q_c. Adaptation of the model to consider the variation of MCP gain with ion energy and type [12] should also be possible. Further consideration of the representation of the ion reflection probability is required to make the model truly useful for low energy, light ions while a deeper understanding of the basic interaction physics is required in order to meaningfully combine the analysis of the high mass response of CsI (Fig. 9) into our model of the working microchannel and produce predictions of the biomolecular response of coated MCPs.

These developments will be addressed in a future contribution.

Acknowledgements

GWF gratefully acknowledges the assistance of Paul Mellor in assembling Table 1 and the patience (which he repeatedly tried) of Keith Birkinshaw, guest editor of this volume.

References

[1] J.A. Panitz, J.A. Foesch, Rev. Sci. Instrum. 47 (1976) 44.
[2] S. Takagi, et al., Nucl. Instrum. Meth. 215 (1983) 207.
[3] R.S. Gao, et al., Rev. Sci. Instrum. 55 (1984) 1756.
[4] M. Hellsing, et al., J. Phys. E 18 (1985) 920.
[5] T. Sakurai, T. Hashizume, Rev. Sci. Instrum. 57 (1986) 236.

[6] A. Muller, et al., Rev. Sci. Instrum. 57 (1986) 349.
[7] M. Hellsing, L. Karlsson, J. Phys. E 19 (1986) 276.
[8] K. Tobita, et al., Jap. J. Appl. Phys. 26 (1987) 509.
[9] O. Almen, et al., J. Phys. E 22 (1989) 382.
[10] S.C. Gujrathi, et al., Nucl. Instrum. Meth. B 64 (1992) 789.
[11] J. Schecker, et al., Nucl. Instrum. Meth. A 320 (1992) 556.
[12] R. Meier, P. Eberhardt, Int. J. Mass Spectrom. 123 (1993) 19.
[13] L. Lundin, U. Rolander, Appl. Surf. Sci. 67 (1993) 459.
[14] A. Bader, et al., Meas. Sci. Tech. 6 (1995) 959.
[15] B. Brehm, et al., Meas. Sci. Tech. 6 (1995) 953.
[16] H.O. Funsten et al., Rev. Sci. Instrum. 67 (1996) 145 and 3478.
[17] G. Westmacott, et al., Nucl. Instrum. Meth. B 108 (1996) 282.
[18] S. Saro, et al., Nucl. Instrum. Meth. A 381 (1996) 5202.
[19] B. Deconihout, et al., Appl. Surf. Sci. 94 (1996) 422.
[20] P.V. Schmidt, et al., Nucl. Instrum. Meth. A 376 (1996) 139.
[21] K.G. Thompson, R.R. Hart, Nucl. Instrum. Meth. A 371 (1996) 563.
[22] J. Oberheide, et al., Meas. Sci. Tech. 8 (1997) 351.
[23] H.C. Straub, et al., Rev. Sci. Instrum. 70 (1999) 4328.
[24] T.M. Stephen, B.L. Peko, Rev. Sci. Instrum. 71 (2000) 1355.
[25] M. Barat, et al., Rev. Sci. Instrum. 71 (2000) 2050.
[26] M.P. Stockli, D. Fray, Rev. Sci. Instrum. 68 (1997) 3053.
[27] J. Mosher, et al., Nucl. Instrum. Meth. A 459 (2001) 532.
[28] D. Twerenbold, et al., Proteomics 1 (2001) 66.
[29] I.S. Gilmore, M.P. Seah, Int. J. Mass Spectrom. 202 (2000) 217.
[30] B.L. Peko, T.M. Stephen, Nucl. Instrum. Meth. B 171 (2000) 597.
[31] G.W. Fraser, Nucl. Instrum. Meth. 206 (1983) 445.
[32] G.W. Fraser, Nucl. Instrum. Meth. 195 (1982) 523.
[33] G.W. Fraser, et al., Nucl. Instrum. Meth. 224 (1984) 272.
[34] R.J. Beuhler, L. Friedman, J. Appl. Phys. 48 (1977) 3928.
[35] E.J. Sternglass, Phys. Rev. 108 (1957) 1.
[36] R.A. Baragiola, et al., Surf. Sci. 90 (1979) 240.
[37] J. Lindhard, M. Schaff, Phys. Rev. 124 (1961) 128.
[38] J. Schou, Phys. Rev. B 22 (1980) 2141.
[39] G. Holmen, Nucl. Instrum. Meth. 185 (1981) 523.
[40] M.V. Zombeck, The Handbook of Space Astronomy and Astrophysics, Cambridge University Press, Cambridge, 1990, p. 365.
[41] S.N. Ghosh, S.P. Khare, Phys. Rev. 125 (1962) 1254.
[42] G.E. Hill, Adv. Electron. Electron. Phys. A 40 (1976) 153; A. Authinarayanan, W.R. Dudding, Adv. Electron. Electron. Phys. A 40 (1976) 167.
[43] V.P. Afanas'ev, D. Naujoks, Z. Phys. B 86 (1992) 39.
[44] T. Mizuno, et al., IEEE Trans. Electron Devices ED-35 (1988) 2323.
[45] G.M. Batanov, Sov. Phys. Solid State 2 (1960) 1839.
[46] E.R. Cawthron, Aus. J. Phys. 24 (1971) 859.
[47] U. Von Gemmingen, Surf. Sci. 120 (1982) 334.
[48] M.J. Higatsberger, et al., J. Appl. Phys. 25 (1954) 883.
[49] G.W. Fraser, Nucl. Instrum. Meth. 206 (1983) 265.
[50] J.C. Baboux, et al., J. Phys. D 4 (1971) 1617.
[51] V. Konig, et al., Int. J. Mass Spectrom. Ion. Phys. 16 (1975) 243.
[52] R. Moshammer, R. Matthaus, J. de Physique C2 (2) (1989) C2–111.
[53] Van Tan Nyugen, K. Wien, Nucl. Instrum. Meth. B 145 (1998) 332.
[54] M. Frank, Nucl. Instrum. Meth. A 444 (2000) 275.
[55] G. Gervasio, et al., Nucl. Instrum. Meth. A 444 (2000) 389.